Nonlocal mechanisms of attosecond interferometry and implications for condensed-phase experiments

Dominik Rattenbacher, Inga Jordan, Axel Schild, and Hans Jakob Wörner*
Laboratorium für Physikalische Chemie, ETH Zürich, Vladimir-Prelog-Weg 2, 8093 Zürich, Switzerland

(Received 27 January 2018; published 20 June 2018)

Attosecond interferometry relies on the application of a train of attosecond extreme-ultraviolet (XUV) pulses and a synchronized low-intensity infrared (IR) field to measure the dynamics of photoemission via the interference signal in the spectrum of emitted electrons. So far, all condensed-phase experiments relying on this technique have investigated metallic, i.e. nontransparent, systems and have revealed the importance of transport and final-state effects. Here, we demonstrate the existence of a nonlocal mechanism of attosecond interferometry general to all condensed-matter systems and particularly important for those that are transparent to the IR. Key to the process is that, after XUV absorption, additional emission pathways result from the absorption or emission of an IR photon at remote positions due to the potential of neighboring atoms (or molecules). By solving the time-dependent Schrödinger equation (TDSE) in one dimension, we show that interference of the resulting local and remote pathways leads to a mapping of the atomic or molecular environment onto the attosecond interference signal. We derive an analytical theory for the local and remote pathways as well as the resulting response and find excellent agreement with the TDSE. Our analytical theory shows that the nonlocal mechanism generally encodes both mean-free paths and scattering delays into the experimental observables. We generalize the analytical theory to the case of multiple collisions and study the effect of path-length distributions typical of electron scattering in condensed matter.

DOI: 10.1103/PhysRevA.97.063415

I. INTRODUCTION

Photoemission is a fundamental phenomenon that entirely takes place on the attosecond timescale. The photoionization dynamics of isolated particles in the gas phase can be described in terms of delays which are defined as the energy derivative of the scattering phase shifts [1,2]. The energy dependencies of scattering phases therefore contain all information necessary to understand photoionization in the time domain. Photoionization delays have been measured in atoms using attosecond streaking [3–5] and attosecond interferometry [6–11] and very recently also in molecules [12]. The theory of attosecond photoionization delays is well developed for atoms [13–19] and first results have also been obtained for molecules [12,20–23].

Photoemission from the condensed phase is considerably more complex. Following the initial emission step, the electron propagates through the condensed-matter environment where it scatters elastically or inelastically off other particles. Each elastic scattering process is characterized by its own complex scattering amplitude $f(\theta,\phi)$, where θ and ϕ describe the polar and azimuthal scattering angle, respectively. The scattering amplitude defines both the associated differential scattering cross section (DCS) $d\sigma/d\Omega = |f(\theta,\phi)|^2$ and the scattering delay $\tau_s = \partial/\partial E \arg(f(\theta,\phi))$, initially discussed by Wigner, Eisenbud, and Smith [1,2]. The total cross section $\sigma = \int |f(\theta,\phi)|^2 \sin\theta d\theta d\phi$, therefore, determines the associated mean-free path $\lambda = 1/(n\sigma)$, with n the number density, and thus the scattering time $t_s = \lambda/v$, where v is the velocity of the particle. We emphasize the difference between the *scattering delay*, caused by a single collision, and the *scattering time*, which is the average time that elapses between two consecutive collisions.

Most previous measurements of photoemission delays from condensed-matter systems have been performed on metals using either the attosecond streaking technique [24,25] based on isolated extreme-ultraviolet (XUV) attosecond pulses [26–28] or attosecond interferometry [29–31], based on XUV attosecond pulse trains [32–34]. In all of these studies, the effect of the IR field on the electrons inside the solids has either been neglected or found to have a minor influence on the measured delays. Since the interaction with the IR field is the "clock", both in attosecond interferometry and in attosecond streaking, this situation explains the primary sensitivitiy of these experiments to the transport time, i.e., the time required by the electron emitted inside the bulk to reach the surface. Considerable theoretical work has also been done on the interpretation of these measurements (see, e.g., Refs. [35–39] and references therein). Both experimental and theoretical work has been reviewed in Ref. [40].

Liquids, dielectrics, and wide-band-gap semiconductors are transparent to the near-infrared radiation (with wavelengths typically centered around 800 nm) used in attosecond interferometry, which leads to a fundamentally different situation than in metals. The electron can interact with the IR field over its entire trajectory. Since the interaction with the IR field acts as the probe, the question naturally arises what timing information is eventually encoded in the measurement. Very recently, attosecond streaking has been employed to measure photoemission delays from SiO_2 nanoparticles. This study

*hwoerner@ethz.ch; www.atto.ethz.ch

concluded, on the basis of a purely classical Monte Carlo trajectory analysis, that the experiment was mainly sensitive to the inelastic scattering times [41].

Here, we present the first fully quantum-mechanical analysis of attosecond interferometry in one-dimensional transparent media with the goal of understanding the relevant temporal information that the method accesses.

We employ a numerical simulation of the time-dependent Schrödinger equation (TDSE) to calculate attosecond interferometry in the simplest possible model potentials representing condensed-matter systems. These calculations reveal a mechanism of attosecond interferometry in which the interactions with the XUV and IR fields take place at spatially separated positions. Following the photoionization of an isolated atom (or molecule), the electron can only exchange photons with the IR field in the immediate vicinity of the parent cation. Energy and momentum conservation forbid the absorption or emission of photons at larger distances because of the absence of a potential gradient. However, in a condensed-matter environment the presence of neighboring atoms or molecules naturally provides potential gradients along the path of the propagating electron. We show that this situation enables an exchange of photons with the IR field, which results in the formation of photoelectron side bands at remote sites. Their interference with the regular local mechanism of attosecond interferometry gives rise to signal contributions that encode details about the scattering dynamics into the observed delays. We rationalize the results of the TDSE by developing an analytical model of these phenomena within the theory of laser-assisted electron scattering (LAES), which enables us to extract a transparent physical picture that will be transferable to the interpretation of both experiments and more advanced three-dimensional calculations. We note that our usage of the term "nonlocal mechanism" is motivated by the fact that the eventually observed electronic response depends on the potentials (and laser electric fields) at local and remote positions.

II. TDSE CALCULATIONS

Figure 1 shows the model potentials used in our study. We chose an attractive Yukawa potential to represent the site from which photoemission takes place. A second Yukawa potential (dotted line) is optionally added at a variable distance r from the attractive well to represent the interaction of the electron with (neutral) neighboring sites. We call this scattering site the "perturber." Throughout the following discussion we use atomic units unless stated otherwise. The total potential therefore takes the form

$$V(x) = -\frac{V_1 e^{-\frac{|x|}{\lambda}}}{\sqrt{x^2+s^2}} + \frac{V_p e^{-\frac{|x-r|}{\lambda}}}{\sqrt{(x-r)^2+s^2}}, \qquad (1)$$

with $V_1 = 1E_h$, $\lambda = 10\,a_0$, $s = 1.2741\,a_0$, and variable V_p. The parameters of the strongly attractive potential [first term in Eq. (1)] were chosen such that the lowest eigenstate [shown in Fig. 1(a)] had a binding energy of 13.61 eV ($0.5E_h$). The TDSE is then solved for an electron exposed to a 40-fs IR pulse centered at 800 nm and a 30-fs XUV attosecond pulse train consisting of harmonic orders $q-1$ and $q+1$ of 800 nm (with q being an even integer). Numerical details on the solution of the TDSE are given in the Supplemental Material [42]. A minimal separation of $r \approx 0.4$ nm was used in all TDSE calculations, such that the binding energy remained unchanged within the quoted accuracy. The results of the analytical theory, discussed in Sec. III, are given for all values of r.

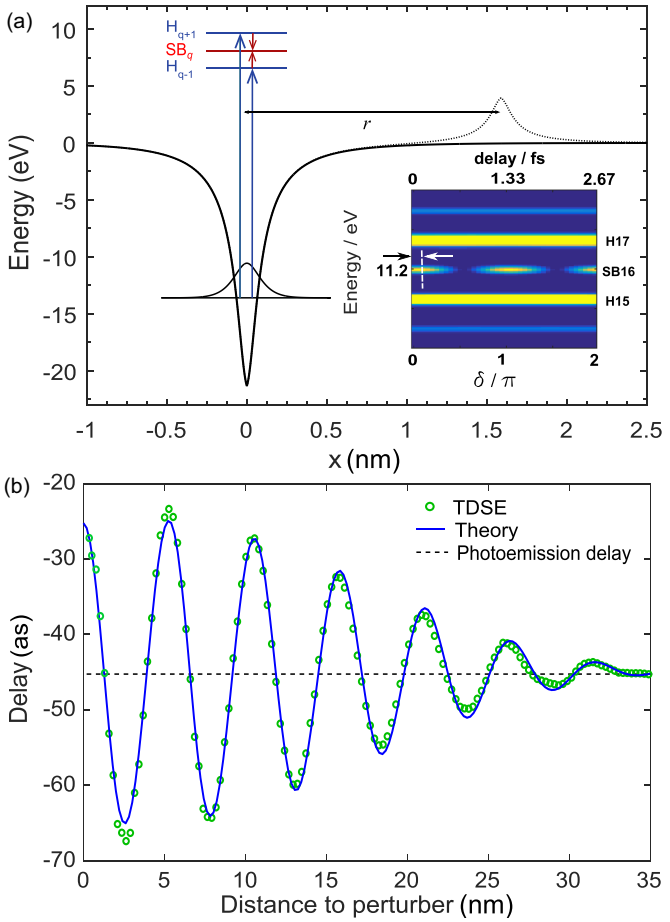

FIG. 1. (a) Model potential employed in solving the TDSE and spectrogram of XUV/IR attosecond interferometry for electrons propagating to the right-hand side using harmonic orders 15 and 17 as a function of the CEP of the IR field (inset). (b) Relative delays between photoemission from the isolated attractive potential and photoemission perturbed by the additional presence of the repulsive potential with $V_p = 4$ eV [dashed line in (a)]. The delays (green circles) have been determined from the phase of the calculated side-band intensity (SB16), shown in panel (a). The full line represents the delay calculated according to Eq. (7).

Both pulse envelopes are cosine-square functions and all spectral phases are chosen to be flat. Instead of varying the offset Δt between the XUV and IR pulses, we continuously scan the carrier-envelope phase (CEP) δ of the IR pulse

$$E = E_0 \cos(\omega t - \delta), \qquad (2)$$

which is equivalent to scanning the offset $\Delta t = \delta/\omega$ between XUV and IR pulses in the continuous-wave limit, but avoids effects related to the envelopes of the two laser pulses. Photoelectron spectra are calculated from the part of the electron wave packet propagating toward $x \to \infty$. An example of such a photoelectron spectrum as a function of the CEP δ (bottom axis) and the associated offset Δt (top axis) is shown in the

inset of Fig. 1(a). The photoelectron spectrum is dominated by two main lines (yellow) that originate from the ionization of the ground state by harmonics 15 and 17. The sideband 16, located between these two lines, displays an intensity oscillation with an angular frequency of 2ω, i.e., a period of 1.33 fs. The analysis of the oscillation phase ϕ (white dashed line) of a given sideband q directly reflects the photoemission delay $\tau = \phi/(2\omega)$ for the case of unchirped pulses.

Figure 1(b) shows the delay obtained from the phase ϕ of the side-band oscillation as a function of the distance r between the photoemission and perturber sites [see Fig. 1(a)]. The delay is found to undergo a periodic beating around a constant value (marked with a dashed line) as a function of the spatial separation between the two Yukawa potentials.

This result clearly contrasts with the Wigner delay of the combined potentials, which would approximately be equal to the sum of the individual Wigner delays of the two potentials and would therefore be independent of the location of the perturbing potential. We show below that the dashed line mainly reflects the Wigner delay of the attractive potential describing the site of photoemission and that the oscillating feature encodes the effect of the environment described by the additional potential. The fast oscillation of this beating has a spatial period of $\pi/(k_{q+1} - k_{q-1})$, where k_n are the wave numbers describing the photoelectron waves emitted by the harmonic of order n. This is the consequence of quantum-mechanical interference between electron wave packets that have propagated with different wave numbers k_{q-1}, k_q, or k_{q+1} before undergoing a transition to the common final state of wave number k_q.

III. ANALYTICAL THEORY

A. General framework

The obtained result cannot be explained in terms of Wigner delays alone. However, it can be fully explained by introducing the existence of "remote" pathways of IR absorption and stimulated emission in addition to the usual "local" pathways (see Fig. 2). In the traditional understanding of attosecond interferometry, the interaction of the XUV and IR fields with the electron wave packet takes place while the latter is still located within the potential of the parent cation. These two local pathways give rise to the purely local process, illustrated in Fig. 2(a), and assumed to be the dominant process in previous work. However, in the presence of neighboring scattering sites, the interaction of the electron wave packet with the IR field can also take place in a different spatial region, leading to remote pathways. In Fig. 2, the top and bottom rows of the panels illustrate the local and remote IR absorption pathways, respectively, whereas the two columns correspond to the local and remote IR stimulated emission pathways. Hence, the "off-diagonals" of the 2×2 panel matrix [Fig. 2(b) and 2(c)] correspond to processes that contain one local and one remote pathway, leading to a nonlocal response. Finally, the process shown in Fig. 2(d) consists of two remote pathways. These three nonlocal processes illustrated in Figs. 2(b)–2(d) arise solely from the presence of a remote potential that enables the absorption or emission of an IR photon in a pathway that is the

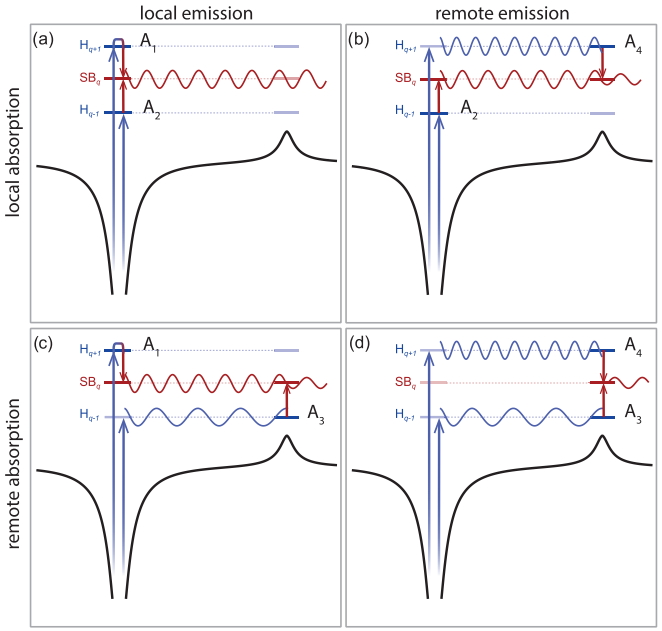

FIG. 2. Illustration of the local (a) and nonlocal (b–d) processes of attosecond interferometry in condensed-matter systems. The blue (long) arrows represents single-photon ionization by an XUV attosecond pulse train. The red (short) arrows represent interaction with the IR field, i.e., absorption or stimulated emission.

one-dimensional analog of laser-assisted electron scattering (LAES)[43].

The expected interference can be calculated analytically as a sum of four quantum-mechanical amplitudes contributing to the signal that is eventually measured in the SB_q state. These contributions are the absorption of a photon from harmonic H_{q+1} and the subsequent stimulated emission of an IR photon either in the cationic potential [with amplitude A_1 in Eq. (3)] or at the perturber potential (A_4), and the absorption of a H_{q-1} photon followed by the IR absorption in the cationic potential (A_2) or during scattering (A_3). The amplitudes A_i of these four pathways are chosen to be real-valued and the corresponding phases are expressed as the sum of contributions from photoemission, free propagation, and scattering. On this basis, the complex second-order amplitude of SB_q can be written as

$$\begin{aligned} c_q^{(2)} = {} & A_1 \exp\left[i\left(\phi^{\mathrm{P}}_{q+1} + \phi_{\mathrm{em}} + \delta + k_q r + \phi^{\mathrm{S}}_q\right)\right] \\ & + A_2 \exp\left[i\left(\phi^{\mathrm{P}}_{q-1} + \phi_{\mathrm{ab}} - \delta + k_q r + \phi^{\mathrm{S}}_q\right)\right] \\ & + A_3 \exp\left[i\left(\phi^{\mathrm{P}}_{q-1} + k_{q-1} r + \phi^{\mathrm{LS}}_{q-1,q} - \delta\right)\right] \\ & + A_4 \exp\left[i\left(\phi^{\mathrm{P}}_{q+1} + k_{q+1} r + \phi^{\mathrm{LS}}_{q+1,q} + \delta\right)\right]. \end{aligned} \quad (3)$$

The phases of the photoemission matrix elements corresponding to harmonic order $q \pm 1$ are represented by $\phi^{\mathrm{P}}_{q\pm1}$. The phase δ denotes the CEP of the IR field as introduced above. The interaction with the IR field during photoemission leads to the additional accumulation of the phases ϕ_{ab} and ϕ_{em}, with values $\phi_{\mathrm{ab}} \approx \phi_{\mathrm{em}} \approx \pi/2$, as verified from the solution of the TDSE and further discussed in the next section. On its way from the photoemission to the scattering site, the electron wave packet travels the distance r, which leads to a propagation phase $k_q r$

for a kinetic energy of $k_q^2/2$. The scattering of the electron wave packet without exchange of energy with the laser field contributes the phase ϕ_q^{S}, whereas scattering accompanied by exchange of energy contributes the phases $\phi_{q\pm1,q}^{\mathrm{LS}}$. Analytical expressions for all phases and amplitudes appearing in Eq. (3) are derived below.

The phases ϕ_{ab} and ϕ_{em} are closely related to the "continuum-continuum" phases ϕ_{cc}, or equivalently the "Coulomb-laser-coupling" phases ϕ_{CLC} discussed in the literature on photoionization delays [15,16] with two main differences. First, ϕ_{cc} does not include the additive quantity $\pi/2$ originating from the interaction with the IR field that is, instead, included in the definition of the two-photon matrix elements [16]. Second, ϕ_{cc} and ϕ_{CLC} are strongly energy dependent because of the long-range character of Coulomb potentials [15,16], whereas ϕ_{ab} and ϕ_{em} are nearly energy independent in our calculations that exclusively use short-range potentials. A similar result has very recently been obtained in the context of photoemission delays from atomic anions [44].

The measurable sideband amplitude is proportional to the squared magnitude of the contributions from all four pathways illustrated in Fig. 2. By grouping all terms without δ-dependence into a constant C, the side-band intensity oscillation is given by

$$\left|c_q^{(2)}\right|^2 = 2\sum_{j=1}^{4} b_j \cos(2\delta + \Delta\phi^{\mathrm{P}} + \varphi_j) + C, \tag{4}$$

where we introduced the difference of photoemission phases $\Delta\phi^{\mathrm{P}} = \phi_{q+1}^{\mathrm{P}} - \phi_{q-1}^{\mathrm{P}}$, and where we defined the products of amplitudes,

$$b_1 = A_1A_2, \quad b_3 = A_1A_3,$$
$$b_2 = A_2A_4, \quad b_4 = A_3A_4,$$

and the angles,

$$\varphi_1 = \phi_{\mathrm{em}} - \phi_{\mathrm{ab}},$$
$$\varphi_2 = (k_{q+1} - k_q)r - \phi_{\mathrm{ab}} - \phi_q^{\mathrm{S}} + \phi_{q+1,q}^{\mathrm{LS}},$$
$$\varphi_3 = (k_q - k_{q-1})r + \phi_{\mathrm{em}} + \phi_q^{\mathrm{S}} - \phi_{q-1,q}^{\mathrm{LS}},$$
$$\varphi_4 = (k_{q+1} - k_{q-1})r + \phi_{q+1,q}^{\mathrm{LS}} - \phi_{q-1,q}^{\mathrm{LS}}.$$

The four δ-dependent terms in Eq. (4) correspond to the four panels of Fig. 2 in the order (a)–(d), i.e., to purely local pathways ($j = 1$), local absorption and remote emission ($j = 2$), local emission and remote absorption ($j = 3$), and to purely remote pathways ($j = 4$). We note that the purely local term does not contain an r-dependence and is thus connected with a constant delay, equal to the photoemission delay.

We now discuss the expected modifications of the delay resulting from the dependence of the signal on the photoemission-perturber distance r. As all four terms in Fig. 4 represent signals that oscillate with $2\delta + \Delta\Phi^P$ and differ only in amplitude and phase, their sum can be written as

$$\left|c_q^{(2)}\right|^2 = A\cos(2\delta + \Delta\phi^{\mathrm{P}} + \phi_{\mathrm{nl}}) + C, \tag{5}$$

with amplitude

$$A^2 = 2\sum_{j=1}^{4}\sum_{k=1}^{4} b_j b_k \cos(\varphi_j - \varphi_k) \tag{6}$$

and phase

$$\phi_{\mathrm{nl}} = \mathrm{atan}\left(\frac{\sum_{j=1}^{4} b_j \sin\varphi_j}{\sum_{j=1}^{4} b_j \cos\varphi_j}\right). \tag{7}$$

In the language of attosecond delays, the photoemission-phase difference $\Delta\phi^{\mathrm{P}}$ yields the photoemission delay $\tau^{\mathrm{P}} = \Delta\phi^{\mathrm{P}}/(2\omega)$, which reflects the properties of the potential from which photoemission takes place.

The phase ϕ_{nl} depends on the distance r to the perturber and collects the contributions from all "non-local" processes, which can therefore be viewed as contributing the additional delay

$$\tau_{\mathrm{nl}} = \frac{\phi_{\mathrm{nl}}}{2\omega}. \tag{8}$$

We now discuss the underlying physical processes in more detail and provide analytical formulas for each of them. For this purpose, we use the one-dimensional scattering amplitude f (for forward scattering) as in Ref. [45],

$$\lim_{|x|\to\infty} \Phi_k(x) \to e^{ikx} + f\left(\frac{x}{|x|}\right)e^{ik|x|}, \tag{9}$$

where $\Phi_k(x)$ is the scattered wave function. We note that different definitions of the scattering amplitude may be used [46].

B. Description of local pathways

The pathways that we designated as local can be described with the theory of the laser-assisted photoelectric effect (LAPE) [47–49]. In this theory, it is assumed that the initial state is a bound state which has a trivial time dependence, that the final state is the laser-dressed state of a free electron in the IR field, and the ionizing laser pulse can be treated as perturbation. Also, the IR field is treated as a continuous wave. Using the LAPE theory, we find that the laser-assisted photoemission amplitude $f_{q+\nu,q}^{\mathrm{LAPE}}$ from state $q+\nu$ to state q is related to the photoemission amplitude to state $q+\nu$ without the assisting IR field, $f_{q+\nu}^{\mathrm{PE}}$, by

$$f_{q+\nu,q}^{\mathrm{LAPE}} \approx e^{i\nu(\pi/2+\delta)} J_\nu\left(\frac{k_q E_0}{\omega^2}\right) f_{q+\nu}^{\mathrm{PE}}. \tag{10}$$

Here, J_ν are the Bessel functions of first kind [50], E is the maximum IR field strength, and k_q is the final wave number of the electron. The parameter ν indicates whether an IR photon was absorbed/emitted ($\nu = -1/1$) or not ($\nu = 0$).

Comparing Eq. (10) with Eq. (3) yields the phases $\Delta\phi^{\mathrm{P}}$, ϕ_{em}, and ϕ_{ab}. Specifically, we have

$$\Delta\phi^{\mathrm{P}} \approx \arg\left(f_{q+1}^{\mathrm{PE}}\right) - \arg\left(f_{q-1}^{\mathrm{PE}}\right), \tag{11}$$

and

$$\phi_{\mathrm{em}} \approx \arg\left[e^{+i\frac{\pi}{2}} J_{+1}\left(\frac{k_q E_0}{\omega^2}\right)\right] \tag{12}$$

$$\phi_{\rm ab} \approx \arg\left[e^{-i\frac{\pi}{2}} J_{-1}\left(\frac{k_q E_0}{\omega^2}\right)\right]. \tag{13}$$

For the laser parameters considered below, we find that

$$\phi_{\rm em} \approx \phi_{\rm ab} \approx \frac{\pi}{2}. \tag{14}$$

C. Description of remote pathways

The nonlocal pathways can be described with the theory of laser-assisted electron scattering (LAES) [43,48]. In this theory, it is assumed that the initial and the final state are laser-dressed states of a free electron in the IR field, that the IR field is a continuous wave, and that the scattering potential can be treated as a perturbation. Using the LAES theory, the laser-assisted scattering amplitude $f^{\rm LAES}_{q+\nu,q}$ can be expressed in terms of the field-free scattering amplitude $f^{\rm ES}_{q+\nu,q}$ as

$$f^{\rm LAES}_{q+\nu,q} \approx e^{i\nu(\frac{\pi}{2}+\delta)} J_\nu\left(\frac{(k_q - k_{q+\nu})E_0}{\omega^2}\right) f^{\rm ES}_{q+\nu,q}, \tag{15}$$

where $k_{q+\nu}$ and k_q are initial and final momenta, respectively. Again, the phase $\pi/2$ in Eq. (15) originates from the choice of the IR field in Eq. (2), and $\nu = -1/1$ corresponds to absorption/emission of a photon, while $\nu = 0$ corresponds to scattering without photon exchange. As we study the influence of the perturber potential [the second part of Eq. (1)] below, we also need the explicit equation for $f^{\rm ES}$ in one dimension,

$$f^{\rm ES}_{q+\nu,q} \approx -\frac{i}{k_q} \langle e^{ik_q r}| \frac{V_p e^{-\frac{|x-r|}{\lambda}}}{\sqrt{(x-r)^2+s^2}} |\Phi_{k_{q+\nu}}\rangle, \tag{16}$$

where $\Phi_{k_{q+\nu}}$ is the scattering wave function of asymptotic momentum $k_{q+\nu}$. With the scattering amplitudes, the phases occurring in Eq. (3) can be expressed as

$$\phi^{\rm LS}_{q-1,q} \approx \arg\left\{e^{-i\frac{\pi}{2}} J_{-1}\left[\frac{(k_q - k_{q-1})E_0}{\omega^2}\right] f^{\rm ES}_{q-1,q}\right\} \tag{17}$$

$$\phi^{\rm S}_{q} \approx \arg\left(f^{\rm ES}_{q,q} + 1\right) \tag{18}$$

$$\phi^{\rm LS}_{q+1,q} \approx \arg\left\{e^{+i\frac{\pi}{2}} J_{+1}\left[\frac{(k_q - k_{q+1})E_0}{\omega^2}\right] f^{\rm ES}_{q+1,q}\right\}. \tag{19}$$

The special form of Eq. (18) is due to the presence of an incoming wave in the channel k_q. For the laser parameters considered below, we find

$$\phi^{\rm LS}_{q-1,q} \approx \arg(f^{\rm ES}_{q-1,q}) + \frac{\pi}{2}, \tag{20}$$

$$\phi^{\rm S}_{q} \approx \arg\left(f^{\rm ES}_{q,q} + 1\right), \tag{21}$$

$$\phi^{\rm LS}_{q+1,q} \approx \arg(f^{\rm ES}_{q+1,q}) - \frac{\pi}{2}. \tag{22}$$

From Eq. (14) we see that in the LAPE, both emission and absorption of an IR photon lead to a phase shift of $\pi/2$ of the field-dressed scattering amplitude compared to the field-free case. In the case of LAES, absorption leads to a phase shift of $+\pi/2$ and emission is accompanied by a phase shift of $-\pi/2$. Comparing the effect of the IR-laser field on the field-free amplitudes, Eqs. (10) and (15), we find that those are identical if we assume that the initial momentum k_i in the LAPE is zero. The difference of the two cases, however, is that $k_f - k_i$ is always positive in the LAPE, while during LAES in forward direction it is positive for absorption and negative for emission of a photon.

IV. DISCUSSION

Based on the results of the analytical theory, it is possible to predict the expected phase shift $\phi = \Delta\phi^{\rm P} + \phi_{\rm nl}$ as a function of the distance r by using Eq. (7) and to compare the result with that of the TDSE. For this purpose, we need to determine the necessary parameters. The photoemission phase $\Delta\phi^{\rm P}$ and the probability of photoemission $|f^{\rm PE}_{q+\nu}|^2$ are obtained from a TDSE propagation of the ground state of the potential Eq. (1) without additional perturber potential. The probabilities $|f^{\rm LAPE}_{q+\nu,q}|^2$ for the LAPE are obtained from Eq. (10). In the case of the LAES pathway, the scattering amplitudes Eq. (15) are obtained numerically by constructing the scattering solutions of the isolated perturber potential and by evaluating the relevant matrix elements given in Eq. (16). This procedure yields the phases $\phi^{\rm S}_q$, $\phi^{\rm LS}_{q-1,q}$, and $\phi^{\rm LS}_{q+1,q}$. The amplitudes A_j are calculated as products of the respective LAPE and LAES amplitudes,

$$A_1 = \left|f^{\rm LAPE}_{q+1,q}\right| 1 + f^{\rm LAES}_{q,q}\left|, \tag{23}\right.$$

$$A_2 = \left|f^{\rm LAPE}_{q-1,q}\right| 1 + f^{\rm LAES}_{q,q}\left|, \tag{24}\right.$$

$$A_3 = \left|f^{\rm LAPE}_{q-1,q-1}\right| f^{\rm LAES}_{q-1,q}\left|, \tag{25}\right.$$

$$A_4 = \left|f^{\rm LAPE}_{q+1,q+1}\right| f^{\rm LAES}_{q+1,q}\left|. \tag{26}\right.$$

By using these values in Eq. (7), we obtain an *ab initio* prediction of the dependence of the phase ϕ and hence of the delay $\tau = \tau^{\rm P} + \tau_{\rm nl}$ on the perturber distance r, as shown in Fig. 1(b) (full blue line).

Figure 3 presents a more extensive comparison of the results from our analytical theory with the TDSE results for two different side-band orders q and for repulsive and attractive remote potentials, i.e., $V_p = +2$ eV or -2 eV. Clearly, the agreement between TDSE and our analytical theory is excellent in all cases. We emphasize that this agreement is obtained without any adjustable parameter.

On the basis of the analytical formula in Eq. (7), we now discuss the origin of the observed beating and the influence of the various parameters. First, we note that the amplitudes A_3 and A_4 of the remote pathways are much smaller than those of the local pathways (A_1 and A_2). In our model calculations, their ratio (remote/local) is approximately 1:10 for $V_p = 4$ eV, on one hand, because the potential from which the electron is emitted was chosen to be much deeper than the perturbing potential and, on the other hand, because the values of the Bessel-type prefactors favor the local LAPE over the remote LAES pathways. In this situation, the term b_1 in Eq. (7) is by far dominant, whereas the terms proportional to b_4 can be neglected. Since in good approximation $A_1 \approx A_2 =: A_{\rm local}$ and $A_3 \approx A_4 =: A_{\rm remote} \ll A_{\rm local}$, we can expand the phase $\phi_{\rm nl}$

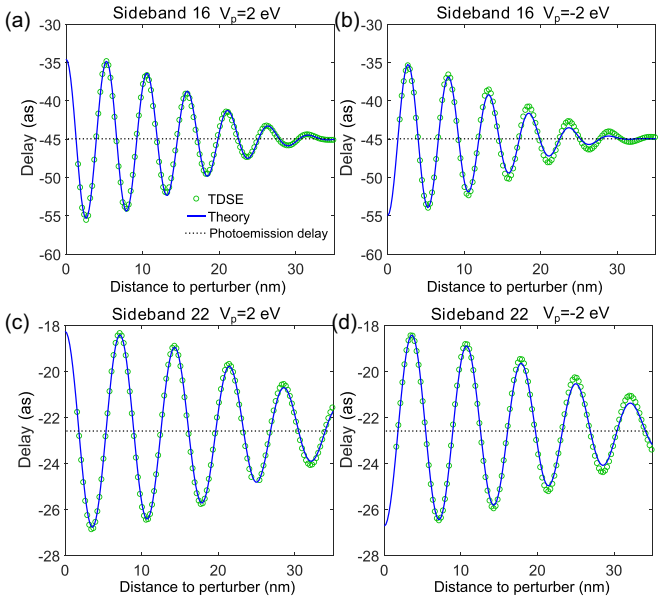

FIG. 3. Comparison of analytical theory (solid blue curves) and TDSE results (green circles) for the side-band orders and V_p values indicated above each figure panel.

Eq. (7) to obtain

$$\phi_{\rm nl} \approx \frac{2A_{\rm remote}}{A_{\rm local}} \sin\left(\frac{\varphi_2+\varphi_3}{2}\right)\cos\left(\frac{\varphi_2-\varphi_3}{2}\right) \tag{27}$$

$$= \frac{2A_{\rm remote}}{A_{\rm local}} \sin((k_{q+1,q}+k_{q,q-1})r + \Delta\phi^{\rm LS}) \times \sin((k_{q+1,q}-k_{q,q-1})r + \Delta\phi^{\rm S}), \tag{28}$$

with

$$\Delta\phi^{\rm LS} = \tfrac{1}{2}\left(\phi^{\rm LS}_{q+1,q} - \phi^{\rm LS}_{q-1,q}\right), \tag{29}$$

$$\Delta\phi^{\rm S} = \tfrac{1}{2}\left(\phi^{\rm LS}_{q+1,q} - 2\phi^{\rm S}_{q} + \phi^{\rm LS}_{q-1,q}\right), \tag{30}$$

$$k_{q+1,q} = \tfrac{1}{2}(k_{q+1} - k_q), \tag{31}$$

$$k_{q,q-1} = \tfrac{1}{2}(k_q - k_{q-1}). \tag{32}$$

Typically, the scattering phases $\arg(f^{\rm ES}_{q+\nu,q})$ differ only little for $\nu = -1, 0,$ or $+1$.

Clearly, the relevant processes for the behavior of the nonlocal phase $\phi_{\rm nl}$ are those illustrated in Figs. 2(b) and 2(c), respectively. The form of Eq. (28) explains the beating patterns observed in Fig. 1(b) and in Fig. 3. It shows that the beating originates from the fact that the electrons travel the distance r to the perturber with different momenta before recombining their paths. Since the energies are directly related to the wave numbers k_i, they accumulate different propagation phases $k_i r$, which give rise to the oscillating delay. The fast oscillation of $\phi_{\rm nl}$ with r Eq. (28) is determined by the oscillation frequency $k_{q+1,q} + k_{q,q-1}$, while the slow oscillation of the envelope is determined by the oscillation frequency $k_{q+1,q} - k_{q,q-1}$.

Inserting the values given in the first row of Table I, we find that for our calculations with $V_p > 0$ $\Delta\phi^{\rm LS} \approx \Delta\phi^{\rm S} \approx \pi/2$, such that both the fast and the slow oscillations are +cosine-like, as seen in Fig. 3(a) [and Fig. 1(b)]. If we change the sign of the perturbing potential, we find $\Delta\phi^{\rm LS} \approx \pi/2$ and $\Delta\phi^{\rm S} \approx -\pi/2$, i.e., the rapid oscillation is still of +cosine type, whereas the envelope is of −cosine type.

TABLE I. Numerical values (in rad) of the relevant phases for photoemission and laser-assisted scattering pertaining to side-band order q and the potentials described in Eq. (1). The phases were chosen to be in the interval $[-\pi,\pi]$.

q	V_p	$\phi^{\rm P}_{q+1} - \phi^{\rm P}_{q-1}$	$\phi^{\rm LS}_{q-1,q}$	$\phi^{\rm S}_{q}$	$\phi^{\rm LS}_{q+1,q}$
16	+2 eV	−0.204	−0.203	−0.378	2.965
16	−2 eV	−0.204	−2.946	0.365	0.171
22	+2 eV	−0.102	−0.144	−0.277	3.008
22	−2 eV	−0.102	−3.000	0.272	0.131

Second, we analyze the maximal amplitude $\tau_{\rm max}$ of the delay $\tau_{\rm nl}$, Eq. (8). For this purpose, we can neglect the fast oscillation with r in Eq. (28), hence

$$\tau_{\rm max} \approx \frac{1}{\omega}\frac{A_{\rm remote}}{A_{\rm local}}, \tag{33}$$

which is located at

$$r_{\rm max} \approx \frac{1}{k_{q+1,q} - k_{q,q-1}}\left[\left(n+\frac{1}{2}\right)\pi - \Delta\phi^{\rm S}\right] \tag{34}$$

for integer n. We note that $\tau_{\rm max}$ is independent of the IR intensity, as in the previously discussed cases of attosecond interferometry. The location of $r_{\rm max}$ with $n = 0$ in our examples above is close to $r = 0$. It follows from Eqs. (20)–(22) that this is in general the case in one-dimensional systems, if the perturber potential can indeed be treated as a perturbation. In this case, the magnitude of the scattering amplitude is small compared to 1, hence Eq. (21) always yields a phase $\phi^{\rm S}_q \approx 0$ and thus $\Delta\phi^{\rm S} \approx \pm\pi/2$, as in our examples. In contrast, if the effect of the incoming channel could be neglected, we would find $\Delta\phi^{\rm S} \approx 0$, and hence $\tau_{\rm nl}$ would be close to zero at $r = 0$.

It is instructive to compare the value of $\tau_{\rm max}$ to the scattering delay of the perturbing potential alone, which is given by

$$\tau_{\rm scat} \approx \frac{1}{2\omega}\left(\phi^{\rm S}_{q+1} - \phi^{\rm S}_{q-1}\right). \tag{35}$$

The quantities $\tau_{\rm max}$ and $\tau_{\rm scat}$ are shown in Fig. 4 as a function of V_p for $q = 16$ and $q = 22$. Interestingly, we find that the

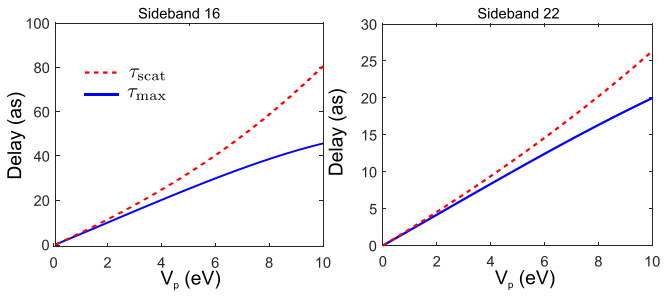

FIG. 4. Comparison of the maximal delay contributed by the nonlocal processes (blue) calculated via Eq. (33) and the scattering delay of the isolated perturber (red) calculated via Eq. (35) for sideband orders 16 (left) and 22 (right).

two types of delays converge to a linear dependence with a common slope for small V_p. Although we illustrate this result only for positive values of V_p, it is clear that it also holds for negative values, i.e., attractive perturbing potentials, since we have seen in Fig. 3 that in this case $\tau_{\max}$ has the opposite sign and so does τ_{scat}. To conclude this section, we have found that the nonlocal processes contribute a maximal delay that scales linearly with V_p for small V_p and is similar to the scattering delay for sufficently small V_p. The linearity of $\tau_{\max}$ and the equality $\tau_{\max} \approx \tau_{\text{scat}}$ represent approximations of improving quality with increasing kinetic energy of the electrons.

V. EFFECT OF MULTIPLE COLLISIONS AND PATH-LENGTH DISTRIBUTIONS

The extension of these results from the considered model system to the condensed phase requires the inclusion of at least two additional effects. First, the number of collisions can be larger than one. Second, the distance traveled by the electron between photoemission and the first collision, or between two consecutive collisions is a distributed quantity, the average of which defines the mean free path.

We first consider the effect of multiple (elastic) collisions. Since we are considering photoelectron spectroscopy as the detection method, we assume that inelastic collisions are associated with a sufficiently large energy loss that the electron is no longer detected within the bandwidth of the investigated sideband. Therefore, since the inelastic mean-free path is usually longer than the elastic mean-free path, on average a finite number of elastic collisions takes place before the first inelastic collision occurs.

We therefore simulate the effect of $n \in 1,\ldots,4$ collisions as a function of the fixed common distance between each of the n perturber potentials. Extending the total second-order amplitude from Eq. (3) to the case of two perturbing potentials separated by the common distance r results in the expression

$$\begin{aligned} c_q^{(2)} = {} & A_1 \exp\left[i\left(\phi_{q+1}^{\mathrm{P}} + \phi_{\mathrm{em}} + \delta + 2k_q r + 2\phi_q^{\mathrm{S}}\right)\right] \\ & + A_2 \exp\left[i\left(\phi_{q-1}^{\mathrm{P}} + \phi_{\mathrm{ab}} - \delta + 2k_q r + 2\phi_q^{\mathrm{S}}\right)\right] \\ & + A_3 \exp\left[i\left(\phi_{q-1}^{\mathrm{P}} + (k_{q-1}+k_q) r + \phi_{q-1,q}^{\mathrm{LS}} - \delta + \phi_q^{\mathrm{S}}\right)\right] \\ & + A_4 \exp\left[i\left(\phi_{q+1}^{\mathrm{P}} + (k_{q+1}+k_q) r + \phi_{q+1,q}^{\mathrm{LS}} + \delta + \phi_q^{\mathrm{S}}\right)\right] \\ & + A_5 \exp\left[i\left(\phi_{q+1}^{\mathrm{P}} + 2k_{q+1} r + \phi_{q+1}^{\mathrm{S}} + \phi_{q+1,q}^{\mathrm{LS}} + \delta\right)\right] \\ & + A_6 \exp\left[i\left(\phi_{q-1}^{\mathrm{P}} + 2k_{q-1} r + \phi_{q-1}^{\mathrm{S}} + \phi_{q-1,q}^{\mathrm{LS}} - \delta\right)\right], \end{aligned} \tag{36}$$

where the symbols ϕ_{q+1}^{S} and ϕ_{q-1}^{S} represent the phase contribution of scattering without exchange of photons with the IR field in the states $q+1$ and $q-1$, respectively. In this case, the amplitudes can be expressed as:

$$A_1 = \left|f_{q+1,q}^{\mathrm{LAPE}}\right|\left|1 + f_{q,q}^{\mathrm{LAES}}\right|^2, \tag{37}$$

$$A_2 = \left|f_{q-1,q}^{\mathrm{LAPE}}\right|\left|1 + f_{q,q}^{\mathrm{LAES}}\right|^2, \tag{38}$$

$$A_3 = \left|f_{q-1,q-1}^{\mathrm{LAPE}}\right|\left|f_{q-1,q}^{\mathrm{LAES}}\right|\left|1 + f_{q,q}^{\mathrm{LAES}}\right|, \tag{39}$$

$$A_4 = \left|f_{q+1,q+1}^{\mathrm{LAPE}}\right|\left|f_{q+1,q}^{\mathrm{LAES}}\right|\left|1 + f_{q,q}^{\mathrm{LAES}}\right|, \tag{40}$$

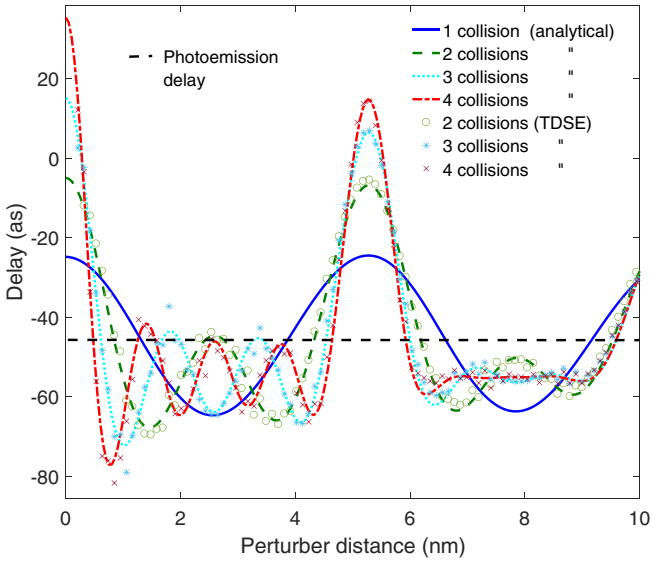

FIG. 5. Effect of multiple collisions separated by a fixed distance between the center of each potential. Repulsive perturbing potentials with $V_p = 4$ eV were used. This figure shows the delay corresponding to SB16.

$$A_5 = \left|f_{q+1,q+1}^{\mathrm{LAPE}}\right|\left|1 + f_{q+1,q+1}^{\mathrm{LAES}}\right|\left|f_{q+1,q}^{\mathrm{LAES}}\right|, \tag{41}$$

$$A_6 = \left|f_{q-1,q-1}^{\mathrm{LAPE}}\right|\left|1 + f_{q-1,q-1}^{\mathrm{LAES}}\right|\left|f_{q-1,q}^{\mathrm{LAES}}\right|, \tag{42}$$

where all symbols have already been defined in Sec. III. This formalism can be readily extended to the case of $n > 2$ scattering events.

Figure 5 shows the numerical results for the cases of n scattering events. For very short distances, the contribution of multiple collisions displays an additive behavior with respect to the total delay. For the present potential parameters with $V_p = +4$ eV, $\tau_{\max} \approx 22$ as. For very short distances, we find in excellent approximation that $\tau \approx \tau^{\mathrm{P}} + n\tau_{\max}$. The overall result of the delay as a function of the distance can immediately be interpreted as the superposition of the "fundamental" oscillation, obtained in the case of a single collision (blue line), with its n higher harmonics. The result is similar to that of a truncated Fourier series, i.e., it displays local maxima of increasing sharpness with increasing number of collisions at the positions where the fundamental oscillation has its maxima. However, just as the blue line actually corresponds to a beating, rather than an oscillation of constant amplitude [see Fig. 1(b)], the other curves also display a weaker second maximum (at 5.3 nm).

We now consider the effect of the path-length distribution. For the sake of simplicity, we begin again by restricting the number of collisions to one and compare three cases. First, the perturber is assumed to be located at a fixed distance r. Second, the distances follow the exponential distribution given by

$$r = \lambda \times \ln\left(\frac{1}{1-x}\right), \tag{43}$$

where x is a random number between 0 and 1 and all four complex amplitudes from Eq. (3) for all r are added coherently.

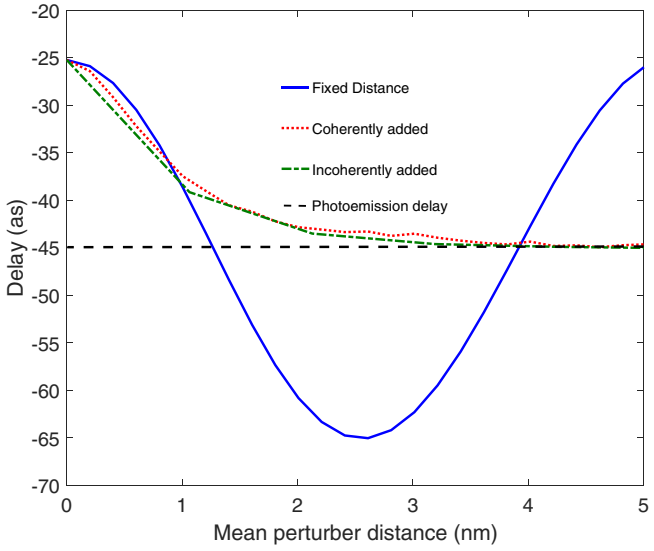

FIG. 6. Comparison between the delay determined from SB16 that emerges if the perturbing potential (with $V_p = 4$ eV) is at a fixed distance (blue line) and if the distance r is distributed according to a mean-free path with coherent addition of the contributions from different r (red) or incoherent addition (green).

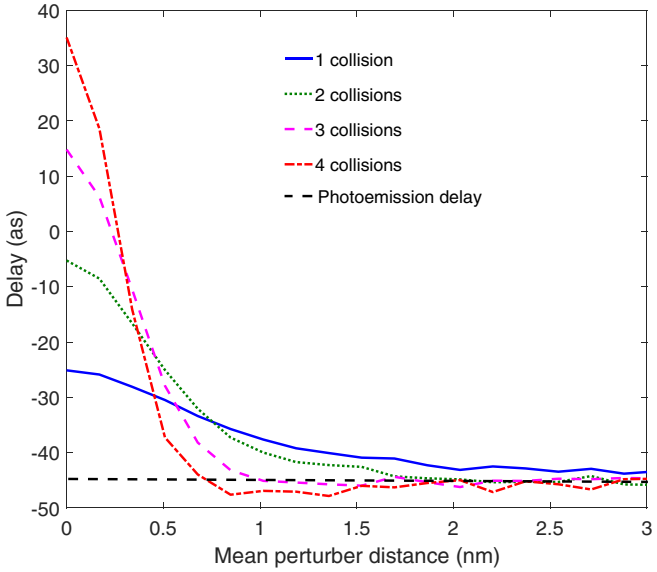

FIG. 7. Dependence of the delay determined from SB16 on the number of collisions and the mean distance between the perturbing potentials (with $V_p = 4$ eV).

Third, the four complex amplitudes for each r are added coherently, but the contributions from different values of r are added incoherently. We note that the path-length distribution given by Eq. (43) corresponds to assuming that the condensed medium has a uniform pair-correlation function.

The results of these three types of calculations are shown as the blue, red, and green curves in Fig. 6, respectively.

In case 1, the familiar beating pattern, similar to Fig. 3(a), is obtained. In cases 2 and 3 the delay is found to rapidly decay toward the value of the photoemission delay with increasing mean perturber distance (or mean-free path). This result has an intuitive interpretation. The superposition of side-band oscillations with different phase shifts leads to a rapid cancellation of the positive and negative contributions of τ_{nl} obtained in case 1, which leads to the observed rapid decay of the effective delay with λ in cases 2 and 3. The difference between coherent and incoherent addition is very minor. The coherently averaged result (case 2) follows the cosine-like behavior of case 1 for very short distances before turning into an exponential-like decay, whereas the incoherently averaged result (case 3) displays the exponential-like decay from the shortest perturber distances. We find that the total delay in the coherently averaged case is well approximated by

$$\tau \approx \tau^{\mathrm{P}} + \frac{\tau_{\max}}{1 + k^2\lambda^2}, \tag{44}$$

where $k = k_{q,q-1} + k_{q+1,q} = (k_{q+1} - k_{q-1})/2$.

Based on Eq. (44), we can distinguish three different regimes. In the limit $\lambda \ll 1/k$ the scattering event will add a delay $\tau_{\max}$ to the intrinsic photoemission delay leading to $\tau = \tau^{\mathrm{P}} + \tau_{\max}$. In the opposite limit $\lambda \gg 1/k$, the effect of scattering on the delays is averaged out, such that the total measured delay is equal to the photoemission delay $\tau = \tau^{\mathrm{P}}$. In the intermediate regime $\lambda \approx 1/k$ the total measured delay will lie between τ^{P} and $\tau^{\mathrm{P}} + \tau_{\max}$ and will therefore be sensitive to both $\tau_{\max}$ and λ.

Finally, we study the simultaneous effect of multiple collisions and the path-length distribution on the observable delay. Figure 7 shows the result of numerical calculations based on our analytical theory for a variable number of collisions (one to four) as a function of λ, using separations between the individual potentials that were all sampled according to Eq. (43). The contributions from all collisions were treated coherently in this calculation to facilitate the comparison with Fig. 5.

For very short mean-free paths, the contribution of multiple collisions displays an additive behavior with respect to the total delay, as expected. We further find that τ decays approximately n times more rapidly with increasing number of collisions n. This behavior can also be expected on the basis of the fixed-distance results in Fig. 5. These results generalize our interpretation of Fig. 6 to the case of multiple collisions.

A complete physical picture of attosecond interferometry in partially transparent media requires three-dimensional simulations. Here, we briefly discuss how the present results from one-dimensional calculations can be applied to a three-dimensional Monte Carlo trajectory simulation. Photoemission or laser-assisted photoemission from multiple locations would be represented by randomly selecting a large number of points inside the material. The propagation of the electron wave packets from each of these points would be represented by a large number of semiclassical trajectories starting from each point. After a random distance r sampled from the distribution given in Eq. (43), scattering or laser-assisted scattering would occur, described by the formalism outlined in the present work. The contributions of all trajectories exiting from the medium would then be added to obtain the simulated side-band oscillation.

VI. CONCLUSIONS

In conclusion, our results demonstrate the importance of nonlocal electron-IR field interactions for attosecond interferometry in the condensed phase. Following photoemission, the liberated electron can either interact with the IR field while it is still within the potential range of the parent cation ("local" pathway) or at a later time when it crosses a remote potential variation created by the presence of another atom or molecule ("remote" pathway). These pathways interfere with each other, resulting in a nonlocal contribution with a periodic dependence of the total observable delay on the separation between the photoemission and scattering sites. The maximal delay is defined by the ratio of the probabilities of the remote to the local pathways, which encodes the depth of the potential describing scattering. For electron kinetic energies significantly larger than the scattering potentials, the maximal delay converges to the scattering delay. When the distances between the perturbers are sampled according to a mean-free path, the contributions of the nonlocal mechanisms to the observed delays decrease rapidly to zero with increasing mean-free path. In the case of short mean-free paths, the observed delay reflects the sum of the elastic scattering delays of all collisions and the photoemission delays. In the case of long mean-free paths, the observed delay is equal to the photoemission delay. Hence, we conclude that attosecond interferometry in one-dimensional transparent amorphous media is, in general, sensitive to both the mean-free paths and the scattering delays. In addition to uncovering the nonlocal mechanism of attosecond interferometry, this work also lays the foundation for treating such processes in three-dimensional media and the corresponding experiments, which will both be the subject of future publications.

ACKNOWLEDGMENTS

We thank Thomas Fennel and Lennart Seiffert for their invaluable contributions to this project, in particular for providing the TDSE code, for running many calculations, for stimulating discussions, and for important improvements to this manuscript. We also thank J. Dahlström, C. Lemell, and J. Burgdörfer for useful discussions. We gratefully acknowledge funding from a Starting Grant of the European Research Council (Contract No. 307270-ATTOSCOPE) and the NCCR-MUST, a funding instrument of the Swiss National Science Foundation.

[1] E. P. Wigner, Phys. Rev. A **98**, 145 (1955).
[2] F. T. Smith, Phys. Rev. **118**, 349 (1960).
[3] M. Schultze *et al.*, Science **328**, 1658 (2010).
[4] M. Sabbar, S. Heuser, R. Boge, M. Lucchini, T. Carette, E. Lindroth, L. Gallmann, C. Cirelli, and U. Keller, Phys. Rev. Lett. **115**, 133001 (2015).
[5] M. Ossiander *et al.*, Nat. Phys. **13**, 280 (2017).
[6] K. Klünder, J. M. Dahlström, M. Gisselbrecht, T. Fordell, M. Swoboda, D. Guénot, P. Johnsson, J. Caillat, J. Mauritsson, A. Maquet, R. Taïeb, and A. L'Huillier, Phys. Rev. Lett. **106**, 143002 (2011).
[7] D. Guénot, K. Klünder, C. L. Arnold, D. Kroon, J. M. Dahlström, M. Miranda, T. Fordell, M. Gisselbrecht, P. Johnsson, J. Mauritsson, E. Lindroth, A. Maquet, R. Taïeb, A. L'Huillier, and A. S. Kheifets, Phys. Rev. A **85**, 053424 (2012).
[8] D. Guénot *et al.*, J. Phys. B **47**, 245602 (2014).
[9] C. Palatchi *et al.*, J. Phys. B **47**, 245003 (2014).
[10] S. Heuser, Á. Jiménez Galán, C. Cirelli, C. Marante, M. Sabbar, R. Boge, M. Lucchini, L. Gallmann, I. Ivanov, A. S. Kheifets, J. M. Dahlström, E. Lindroth, L. Argenti, F. Martín, and U. Keller, Phys. Rev. A **94**, 063409 (2016).
[11] I. Jordan, M. Huppert, S. Pabst, A. S. Kheifets, D. Baykusheva, and H. J. Worner, Phys. Rev. A **95**, 013404 (2017).
[12] M. Huppert, I. Jordan, D. Baykusheva, A. von Conta, and H. J. Wörner, Phys. Rev. Lett. **117**, 093001 (2016).
[13] A. S. Kheifets and I. A. Ivanov, Phys. Rev. Lett. **105**, 233002 (2010).
[14] S. Nagele *et al.*, J. Phys. B **44**, 081001 (2011).
[15] R. Pazourek, J. Feist, S. Nagele, and J. Burgdörfer, Phys. Rev. Lett. **108**, 163001 (2012).
[16] J. M. Dahlström, A. L'Huillier, and A. Maquet, J. Phys. B **45**, 183001 (2012).
[17] J. Dahlström *et al.*, Chem. Phys. **414**, 53 (2013).
[18] A. S. Kheifets, Phys. Rev. A **87**, 063404 (2013).
[19] A. Maquet, J. Caillat, and R. Taïeb, J. Phys. B **47**, 204004 (2014).
[20] I. A. Ivanov, A. S. Kheifets, and V. V. Serov, Phys. Rev. A **86**, 063422 (2012).
[21] P. Hockett, E. Frumker, D. M. Villeneuve, and P. B. Corkum, J. Phys. B **49**, 095602 (2016).
[22] D. Baykusheva and H. J. Wörner, J. Phys. B **50**, 078002 (2017).
[23] D. Baykusheva and H. J. Wörner, J. Chem. Phys. **146**, 124306 (2017).
[24] J. Itatani, F. Quéré, G. L. Yudin, M. Y. Ivanov, F. Krausz, and P. B. Corkum, Phys. Rev. Lett. **88**, 173903 (2002).
[25] R. Kienberger *et al.*, Nature **427**, 817 (2004).
[26] A. L. Cavalieri *et al.*, Nature **449**, 1029 (2007).
[27] S. Neppl, R. Ernstorfer, E. M. Bothschafter, A. L. Cavalieri, D. Menzel, J. V. Barth, F. Krausz, R. Kienberger, and P. Feulner, Phys. Rev. Lett. **109**, 087401 (2012).
[28] S. Neppl *et al.*, Nature **517**, 342 (2015).
[29] V. Véniard, R. Taïeb, and A. Maquet, Phys. Rev. A **54**, 721 (1996).
[30] P. M. Paul *et al.*, Science **292**, 1689 (2001).
[31] H. Muller, Appl. Phys. B **74**, s17 (2002).
[32] R. Locher *et al.*, Optica **2**, 405 (2015).
[33] M. Lucchini, L. Castiglioni, L. Kasmi, P. Kliuiev, A. Ludwig, M. Greif, J. Osterwalder, M. Hengsberger, L. Gallmann, and U. Keller, Phys. Rev. Lett. **115**, 137401 (2015).
[34] Z. Tao *et al.*, Science **353**, 62 (2016).
[35] C.-H. Zhang and U. Thumm, Phys. Rev. Lett. **102**, 123601 (2009).
[36] C. Lemell, B. Solleder, K. Tökési, and J. Burgdörfer, Phys. Rev. A **79**, 062901 (2009).
[37] J. C. Baggesen and L. B. Madsen, Phys. Rev. A **80**, 030901 (2009).

[38] A. G. Borisov, D. Sánchez-Portal, A. K. Kazansky, and P. M. Echenique, Phys. Rev. B **87**, 121110 (2013).
[39] Q. Liao and U. Thumm, Phys. Rev. A **89**, 033849 (2014).
[40] R. Pazourek, S. Nagele, and J. Burgdörfer, Rev. Mod. Phys. **87**, 765 (2015).
[41] L. Seiffert *et al.*, Nat. Phys. **13**, 766 (2017).
[42] See Supplemental Material at http://link.aps.org/supplemental/10.1103/PhysRevA.97.063415 for a brief description of the numerical details concerning the solution of the TDSE.
[43] N. M. Kroll and K. M. Watson, Phys. Rev. A **8**, 804 (1973).
[44] E. Lindroth and J. M. Dahlström, Phys. Rev. A **96**, 013420 (2017).
[45] J. H. Eberly, Am. J. Phys. **33**, 771 (1965).
[46] V. E. Barlette, M. M. Leite, and S. K. Adhikari, Am. J. Phys. **69**, 1010 (2001).
[47] F. H. Faisal, J. Phys. B **6**, L89 (1973).
[48] L. B. Madsen, Am. J. Phys. **73**, 57 (2005).
[49] A. J. Galán, L. Argenti, and F. Martín, New J. Phys. **15**, 113009 (2013).
[50] Instead of $J_\nu(\frac{k_q E_0}{\omega^2})$, it is also possible to use $J_\nu(\frac{k_q E_0}{\omega^2}, \frac{E_0^2}{8\omega^3})$, with $J_\nu(x, y)$ being the generalized Bessel functions, cf. Ref. [48]